Energy &
Environmental
Science

rsc.li/ees

Volume 11
Number 4
April 2018
Pages 719-1000

ISSN 1754-5706

ROYAL SOCIETY
OF CHEMISTRY

REVIEW ARTICLE
Yuekun Lai, Zhiqun Lin et al.
Graphene aerogels for efficient energy storage and conversion

ROYAL SOCIETY
OF CHEMISTRY

rsc.li/ees

Broader context

Aqueous zinc-iodine batteries feature high safety, large volumetric energy density, and cost-effectiveness, making them well-suited for grid-scale energy storage devices. However, their practical implementation is highly hampered by the rampant Zn dendrite growth, polyiodide shuttling, and interfacial side reactions. To solve this dilemma, we provide a facile strategy, constructing a cation-selective artificial layer on Zn anode based on the amorphous $Na_2Zn_2(TeO_3)_3$. It possesses the periodic ion channels and anion skeleton, while exhibits broaden ion channels and shorten the ion diffusion pathways that compared to the crystalline counterpart. Benefit from the rapid and cation-selective ion flux enabled by the amorphous $Na_2Zn_2(TeO_3)_3$ layer, the stability of Zn platting/striping process is achieved, especially for the superior cycle performance of the high loading zinc-iodine pouch battery. This work emphasizes the importance of structural innovation of the interface material in promoting the aqueous zinc-ion batteries.

ARTICLE

Amorphous anion skeletons induced rapid and cation-selective ion flux towards stable aqueous zinc-iodine batteries

Zhenjing Jiang[a,b], Zijuan Du[c], Kailin Luo[a], Yanfei Zhang[d], Hang Yang[b], Wei Zhang[b], Ruwei Chen[b], Jie Chen[b], Zhe Cui[b], Fuhan Cui[a], Rui Pan[a], Guoju Zhang[a], Shuangying Lei[a], Litao Sun[a], Kuibo Yin[a,*], Guanjie He[b,*]

The aqueous zinc-iodine battery is considered as a promising technology for large-scale energy storage due to its high safety, large energy density, and easy accessibility. However, its development suffers from two challenges: parasitic side reactions on the Zn anode and the polyiodide shuttling effects. To overcome them, we designed an artificial protective layer on the Zn anode based on the amorphous zeolite-like $Na_2Zn_2(TeO_3)_3$, whose crystalline counterpart possesses the periodic ion channels and anion skeleton. It not only preserves the original coordination environments and pore structures of the crystalline counterpart, but also exhibits the broaden ion channels and shorten the ion diffusion pathways. Combining the superior structural stability of the amorphous $Na_2Zn_2(TeO_3)_3$, the Zn anode can stable cycle for 2,790 h at 1 mA cm^{-2} with a low overpotential. Meanwhile, the $Zn_2(TeO_3)_3^{2-}$ anion skeleton can also repel I$^-$-species and SO_4^{2-} anions from the anode surface, thus enabling outstanding Zn plating/stripping reversibility and excellent cyclic ability of the full cells coupled with different cathodes. Significantly, the capacity retention of the high mass loading zinc-iodine pouch cell could arrive 92.7% after 600 cycles. This work provides a novel strategy to achieve high-performance zinc-iodine batteries and holds great promise for its practical applications.

Broader context

Aqueous zinc-iodine batteries feature high safety, large volumetric energy density, and cost-effectiveness, making them well-suited for grid-scale energy storage devices. However, their practical implementation is highly hampered by the rampant Zn dendrite growth, polyiodide shuttling, and interfacial side reactions. To solve this dilemma, we provide a facile strategy, constructing a cation-selective artificial layer on Zn anode based on the amorphous $Na_2Zn_2(TeO_3)_3$. It possesses the periodic ion channels and anion skeleton, while exhibits broaden ion channels and shorten the ion diffusion pathways that compared to the crystalline counterpart. Benefit from the rapid and cation-selective ion flux enabled by the amorphous $Na_2Zn_2(TeO_3)_3$ layer, the stability of Zn platting/striping process is achieved, especially for the superior cycle performance of the high loading zinc-iodine pouch battery. This work emphasizes the importance of structural innovation of the interface material in promoting the aqueous zinc-ion batteries.

Introduction

In the backdrop of the global energy crisis, the green transformation of energy through developing sustainable energy sources, e.g., wind and solar energy, has become urgent.[1–3] The wide application of reliable grid-scale energy storage instruments is indispensable to enhance their utilization.[4] Nowadays, lithium-ion batteries are the mainstream electrochemical energy storage technology because of their substantial energy density and low self-discharge rate.[5] However, the limited lithium resources and high flammability of electrolytes severely hinder their commercial application in stationary energy storage systems. Therefore, it is crucial to develop other energy storage technologies that feature abundant resources and high safety for substitution, e.g., aqueous aluminum-ion, aqueous sodium-ion, and aqueous magnesium-ion batteries.[6–9] Aqueous zinc-ion batteries are considered a promising energy storage technology due to the high volumetric capacity of 5,188 mAh cm^{-3}, low redox potential (−0.72 V vs. standard hydrogen

electrode), abundance of the anode.[10,11] Furthermore, the non-flammable and environment-friendly aqueous electrolytes also enable the easy fabrication, making them particularly suitable for grid-scale energy storage.[12] For the cathode materials, iodine (I$_2$) has garnered widespread attention due to its high theoretical capacity and abundance of raw materials, particularly the high discharge potential plateau of 1.38 V vs. Zn^{2+}/Zn, enabling batteries to achieve a high energy density of 220 Wh kg$_{iodine}^{-1}$ (based on the reversible conversion between I$^-$ and I^0).[13,14] However, the practical application of zinc-iodine batteries is hindered by uncontrollable parasitic reactions on the Zn metal anode (e.g., hydrogen evolution reaction, corrosion, and dendrite growth) and the shuttle effect of the iodine cathode.[15-17] Consequently, the battery would generally cycle with low Coulombic efficiency (CE) and suffer from rapid short-circuit.

By now, numerous efforts have been made to endow the practical feasibility of aqueous zinc-iodine batteries, including polyiodide shuttling elimination, iodine species confinement, and Zn metal anode protection.[18-20] Among them, protecting the Zn metal anode is rather crucial as the I$^-$ species in the electrolyte also accelerate the performance decay of the anode. However, the simultaneous realization of fast Zn^{2+} ion transport and long-term cycling stability of the battery remains a significant challenge.[21,22] The most common approach is using ion-selective membranes that allow positively charged Zn^{2+} ions to pass through while preventing the diffusion of high-concentration I$_3^-$ from the I$_2$ cathode to the Zn anode.[16,23,24] For example, Nation membranes are widely applied in zinc-iodine batteries because of their reliable cation-selective performance, attributed to the electrostatic repulsion effect generated by rich immobilized sulfonic acid groups.[25] Nevertheless, the Nation membranes typically have narrow and torturous ion transport channels, thus generally delivering sluggish electrochemical

a. SEU-FEI Nano-Pico Center, Key Laboratory of MEMS of Ministry of Education, Southeast University, Nanjing 210096, P.R. China. E-mail: yinkuibo@seu.edu.cn

b. Christopher Ingold Laboratory, Department of Chemistry, University College London, London WC1H 0AJ, UK. E-mail: g.he@ucl.ac.uk

c. State Key Laboratory of Silicate Materials for Architectures, Wuhan University of Technology, Wuhan 430070, P.R. China.

d. School of Materials Science and Engineering, Qilu University of Technology, Jinan 250353, China.

†Electronic Supplementary Information (ESI) available. See DOI: 10.1039/x0xx00000x

reaction kinetics due to the anion-repelled ion migration behavior.[26] On the other hand, the pore engineering of porous polyolefin/carbon and metal-organic frameworks (MOFs, e.g., UiO-66 and Zn-BTC, with a diameter of 0.6 and 0.5 nm, respectively) are also reported to effectively block the large hydrated I_3^- ion.[27,28] In addition, they can also exclude water molecules of hydrated Zn^{2+} ions and uniformize Zn^{2+} ion flux at the interface to stabilize the Zn anode. Regretfully, the structural stability of the ion diffusion channels of MOFs and other porous materials in aqueous electrolytes needs further improvement. Particularly, the charge/discharge processes would generate an alkaline environment at the anode interface due to the violent HER, thus accelerating the failure and block of those functional interlayers.[29] That is, searching for an interfacial material with wide ion transport channels and high structural stability, capable of long-term blockage of I_3^- and rapid Zn^{2+} ion flux, is essential for the application of zinc-iodine batteries in grid-scale energy storage applications.

The zemannite crystals are typically consistent with $A_{2-x}[M_2(TeO_3)_3]\cdot nH_2O$ (A = Na, K, Rb, Cs; M = Mn, Co, Ni, Cu, Zn). They are made up of an anionic $[M_2(TeO_3)_3]^{2-}$ framework and is permeated by large and hexagonal channels (about 0.82 nm) extending along [001] direction.[30,31] Because of the larger structural frameworks and channel size, we chose $Na_2Zn_2(TeO_3)_3$ crystal to construct a protective layer on the Zn metal anode,

which has the potential to facilitate the Zn^{2+} ion transport process.[31] After heat treatment, the crystalline $Na_2Zn_2(TeO_3)_3$ is confirmed to transform into an amorphous one with preserved coordination environments and pore structures. The amorphous $Na_2Zn_2(TeO_3)_3$ shows an enhanced structural stability and shortened ion diffusion pathway (along the lone pairs of electrons of the TeO_3 unites), thereby enabling the Zn||Zn symmetric cell a lifespan of 2,790 h with a low and stable overpotential. In addition, the presence of $Zn_2(TeO_3)_3^{2-}$ anion skeleton can also repulse SO_4^{2-} and I_3^- anions at the anode interface, thus effectively suppressing the corrosion and surface passivation of the Zn anode. Consequently, the amorphous $Na_2Zn_2(TeO_3)_3$ interlayer enables a high CE of 99.6% of the Zn||Cu half-cell, while the Zn||MnO$_2$ full-cells with limited Zn provided (N/P ratio arrives 2.6, closely to the practical application level) could stable cycle for more than 620 cycles with little capacity decay. Especially, when assembled into a high loading Zn||I$_2$ pouch cell, it can still stable cycle for 600 times with a capacity retention of 92.7%, is among the most stable cycling performances to date. That is, the amorphous $Na_2Zn_2(TeO_3)_3$ interlayer can not only push the aqueous zinc-ion batteries towards practical application but also promote the development of other electrochemical devices based on the selective ion diffusion mechanism.
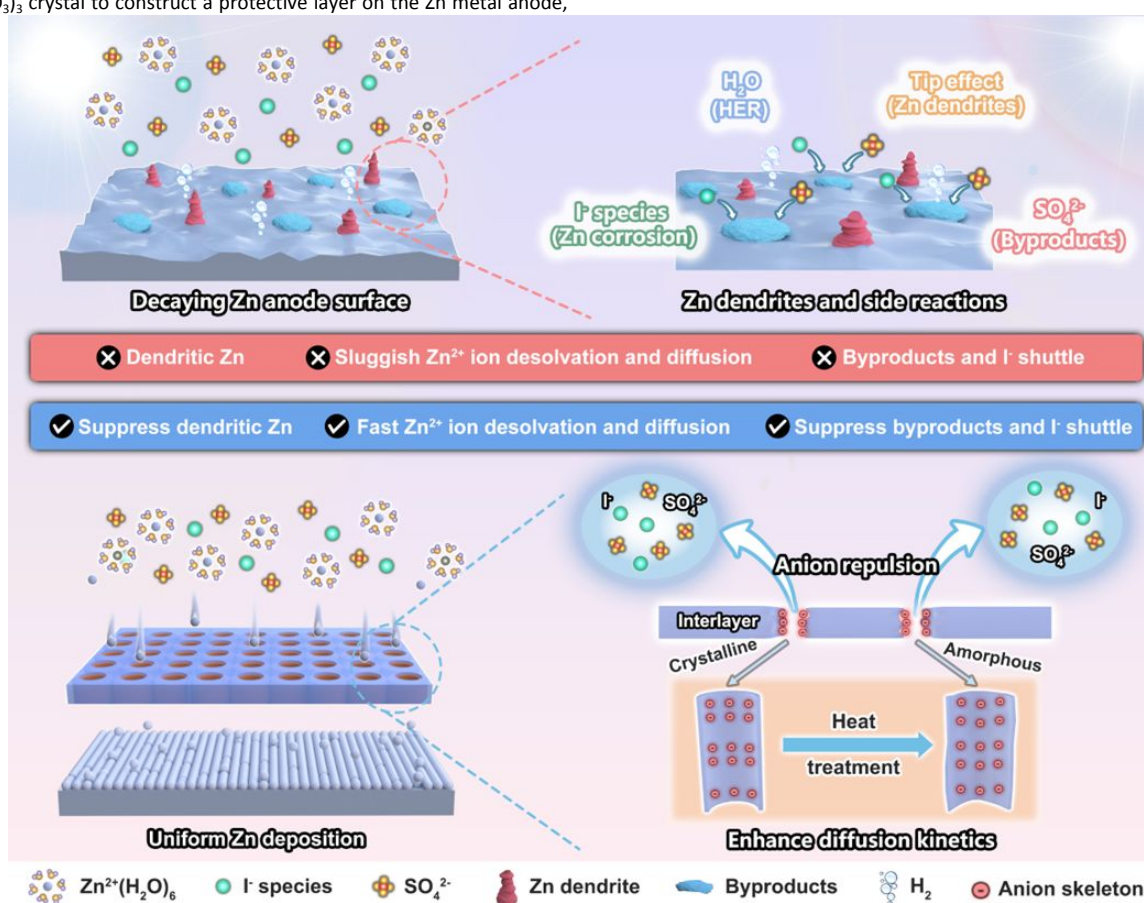
Scheme 1. Illustrate the role of the artificial interlayer based on the anion skeleton in inhibiting Zn dendrite and other side reactions on the Zn anode and its amorphous transform in enhancing ion diffusion kinetics.

Results and discussion

### Characterization of Crystalline and Amorphous Samples

The crystalline $Na_2Zn_2(TeO_3)_3$ (named CNZT) powder was prepared through a facile solvothermal method and then heated at 453 K under Ar atmosphere to acquire the amorphous one, which is named ANZT. As exhibited in Fig. 1a, the X-ray powder diffractometer (XRD) patterns show that all diffraction peaks of the as-prepared CNZT sample resemble the $Na_2Zn_2(TeO_3)_3$ (ICSD No:97-003-3638). Those diffraction peaks disappeared after heat treatment,

indicating the crystalline NZT powder was transformed into an amorphous one. Both the CNZT and ANZT samples are highly stable, as their crystalline and amorphous states were preserved after ball milling with PVDF followed with the drying process at 375 K for 24 h. To clarify the crystalline-amorphous transform progress of CNZT powder, the differential scanning calorimetry (DSC) measurement was carried out. Clearly, the weight loss of the sample begins at 308 K, which is accompanied by the endothermic peak in the DSC up-scan curve (Fig. 1b). That is, the amorphous transformation process is mainly induced by the loss of water molecules in the channels of CNZT samples.[32]

ARTICLE
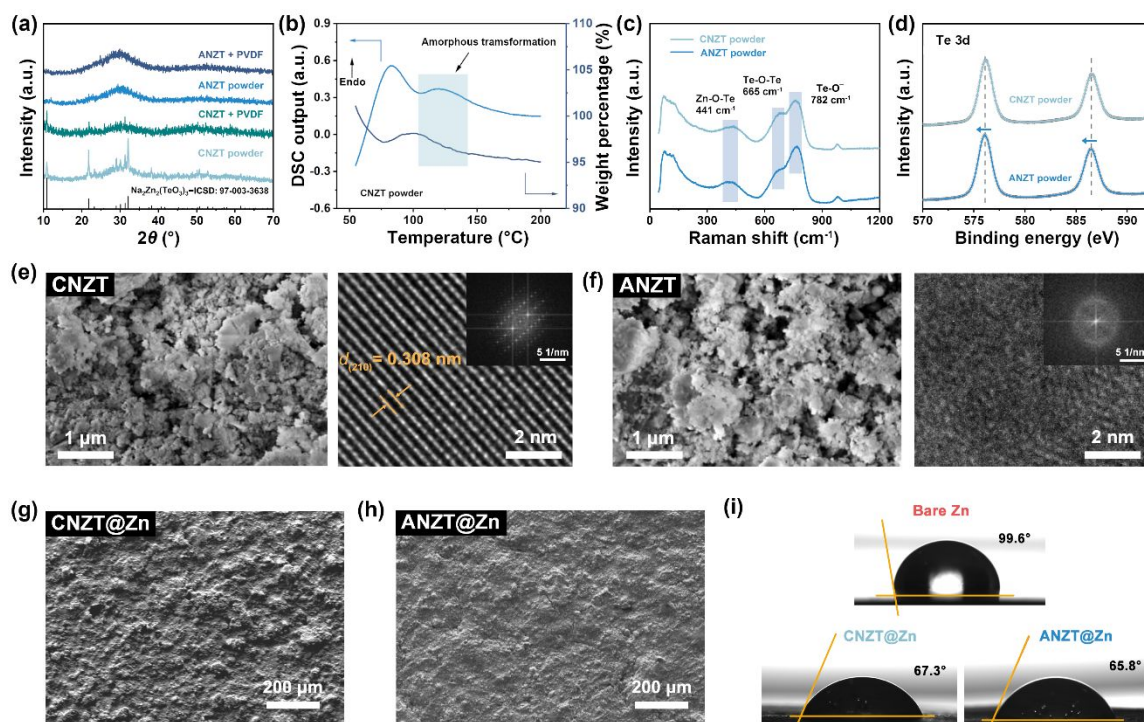
Fig. 1 (a) XRD patterns of CNZT powder, ANZT powder, CNZT interlayer, and ANZT interlayer. (b) DSC up-scan and weight loss curves of the CNZT powder. (c) Raman spectra of CNZT and ANZT powders. (d) High resolution XPS spectra of Te 3d of ANZT and CNZT powders. SEM images of (e) CNZT and (f) ANZT powders and corresponding HRTEM images with SAED results. SEM images of prepared (g) CNZT and (h) ANZT interlayers. (i) The contact angles of different Zn anodes to the 2 M ZnSO$_4$ electrolyte.

To detect the structure evolution of the crystalline sample during the heat-treatment process, the Raman spectra of the CNZT and ANZT powders were acquired. As shown in Fig. 1c, the bands at 441 cm^{-1}, 665 cm^{-1}, and 782 cm^{-1} belong to the bending motion of O in the Zn–O–Te/Te–O–Te asymmetric stretching, and the Te–O$^-$ stretching, respectively.[33] In addition, their Fourier transform infrared spectroscopy (FTIR) spectra (Fig. S1a, ESI†) also show identical peak locations of about 590 cm^{-1} and 643 cm^{-1}, corresponding to the Zn–O and Te–O bonds, respectively.[34] Meanwhile, in high-resolution XPS spectra of O 1s and Te 3d spectra, signal peaks of CNZT and ANZT exhibit similar locations and shapes, indicating the same coordination environment around their O and Te atoms (Figs. 1d and S1b,c, ESI†). These peaks are slightly blue-shifted in the ANZT compared to the CNZT, implying the longer Te–O and Zn–O bonds in the ANZT powder, which will be discussed later. The BET analysis also shows that the CNZT and ANZT powders possess similar BET surface area, pore volume, and pore distribution (Fig. S2, ESI†). These above results confirm the chemical composition and coordination environment of CNZT is preserved during the heat treatment, which can be confirmed by the inductively coupled plasma (ICP) results in Table S1, ESI†.

In addition, the scanning electron microscope (SEM) images and energy dispersive spectrometer (EDS) results (Fig. S3, ESI†) shows both the CNZT and ANZT samples consist of small particles with the uniformly distributed Na, O, Te, and Zn elements. Besides, those small particles in ANZT are slightly agglomerate during amorphization process. The selected-area electron diffraction (SAED) results confirm the highly ordered single-crystalline hexagonal arrangement as characterized by the Na$_2$Zn$_2$(TeO$_3$)$_3$ (210) plane with a crystalline interplanar spacing of 0.308 nm in the high-resolution transmission electron microscopy (HRTEM) image, as shown in Fig. 1e. However, for the ANZT sample, no periodic lattice fringes are observed (Fig. 1f), which is in good agreement with the XRD results.

Both the prepared CNZT and ANZT interlayer on Zn anode delivers smooth and compact morphology, thereby ensuring the protection effect for the Zn metal anode (Figs. 1g,h). Meanwhile, their side-view SEM images are acquired

to determine the thickness of prepared CNZT and ANZT interlayers (Fig. S4, ESI†), which also proves that both the prepared interlayers are compact. The electrolyte wettability of those interlayers between the Zn metal anode and the electrolyte was also essential to the interfacial ion transport process. As displayed in Fig. 1i, both the CNZT (67.3°) and ANZT (65.8°) interlayer exhibit the relatively low contact angle to 2 M ZnSO$_4$ electrolyte, which of bare Zn anode is 99.8°, thus facilitating the Zn^{2+} ion transport kinetics at anode interface.[35] The hardness of CNZT and ANZT interlayers are also compared by nanoindentation measurement. As shown in Fig. S5 (ESI†), the interlayer with CNZT shows low hardnesses of 148.1, 168.3, and 99.3 GPa at the three selected positions. In contrast, the amorphous one delivers high hardnesses of 185.2, 197.8, and 200.3 GPa, thereby enabling the stability of the prepared interface during cycling.[36] In this work, the thickness of used Zn anode is 50 μm unless otherwise noted.

## The Enhanced Ion Transport Kinetics in ANZT Interlayer

The detailed local structures of CNZT and ANZT samples were studied through the classical molecular dynamic simulation (MD) simulation. Based on the corresponding structural models, the radial distribution function (RDF) curves were acquired. Clearly, the Te-O coordination distance increased from 1.85 Å (CNZT) to 1.95 Å (ANZT), as displayed in Fig. 2a. According to the structural model of CNZT, the ion transport channels are formed by the alternating connection of TeO$_3$ and ZnO$_4$ units. Therefore, the increased Te–O distance in ANZT indicates the enlargement of the radius of those ion transport channels. In addition, the contained Na$^+$ ion in the hexagonal channels extending along [001] direction that consist of the anionic [Zn$_2$(TeO$_3$)$_3$]$^{2-}$ framework is known to can exchanged with the external metal ions.[30] Therefore, we propose that the Zn^{2+} ions in electrolyte will also replace the Na$^+$ ions in those channels during cycling (Fig. S6c, ESI†). To confirm this, the high-resolution Na 1s XPS spectra of CNZT and ANZT interlayers before and after cycles were acquired and compared. As shown in Fig. S6d, ESI†, the peaks of Na 1s XPS spectra of ANZT and CNZT interlayers are located at about 1071 eV (belong to Na$^+$ ion), both disappear after cycling, implying the loss of Na$^+$ ions in the channels.

ARTICLE
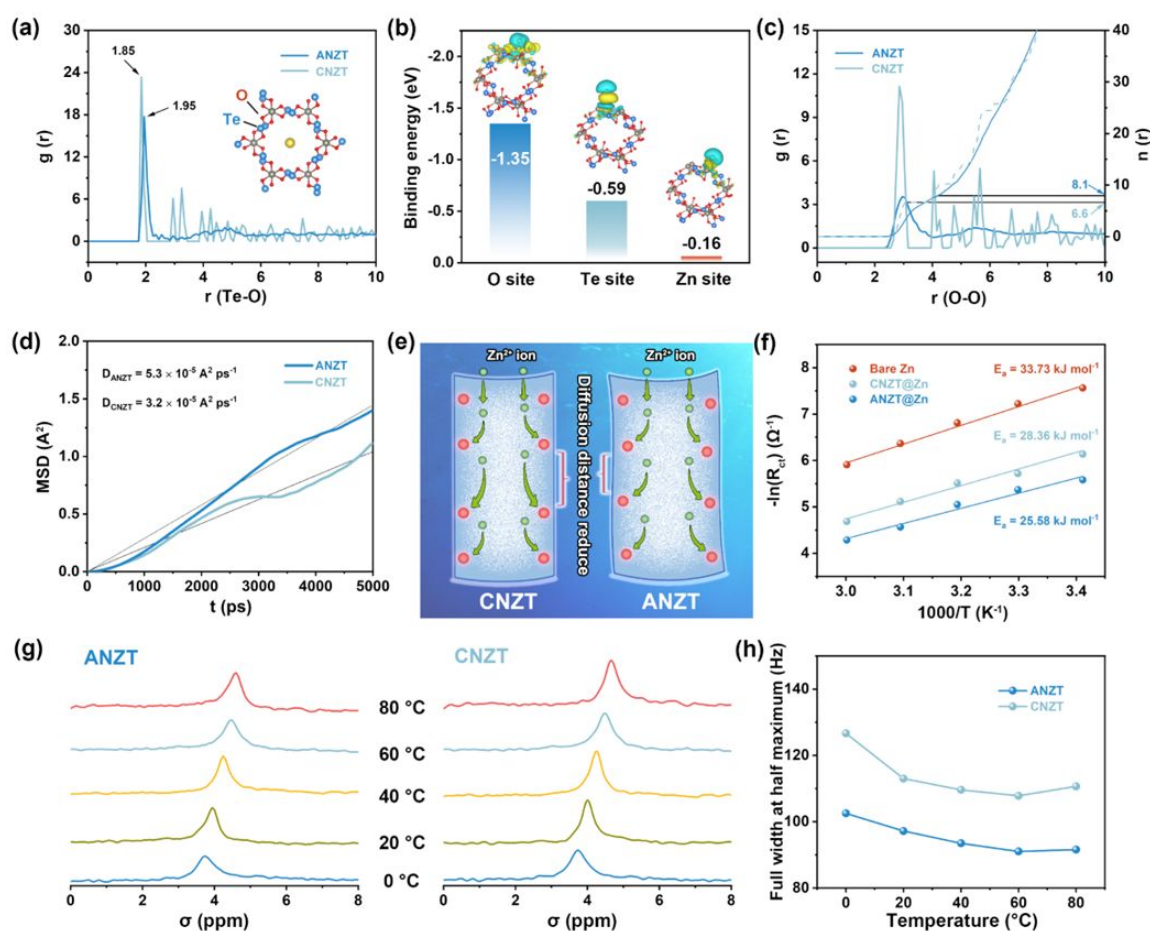
Fig. 2 (a) The radial distribution function (RDF) curves of Te-O distance of CNZT and ANZT samples that are based on classical molecular dynamics simulation, insert: corresponding structural model of $Na_2Zn_2(TeO_3)_3$ crystal. (b) Calculated binding energies between the O, Te, and Zn sites of CNZT toward the adsorbed Zn atom with the corresponding charge difference pictures. (c) The RDF and coordination number curves of O–O distance of CNZT and ANZT samples (based on classical molecular dynamics simulation). (d) The mean square displacements (MSD) results of Zn^{2+} ions in the channels of CNZT and ANZT samples. (e) A schematically illustrate the reason for the faster Zn^{2+} ion transport kinetics in ANZT compared to CNZT samples. (f) The calculated activation energy for hydrated Zn^{2+} ions in the electrolyte to deposit on bare Zn, CNZT@Zn, and ANZT@Zn anodes. (g) Temperature-varied ^{23}Na NMR spectra of ANZT and CNZT samples. (h) The full width at half maximum of the peaks in ^{23}Na NMR spectra of different samples.

On the other hand, the Zn^{2+} ion diffusion path in the channels is determined by the DFT calculation (Fig. 2b). Specifically, the O site (−1.35 eV) in the channel shows the strongest interaction with the adsorbed Zn atom, which for Te site and Zn site to Zn atom are −0.59 eV and −0.16 eV, respectively. Consequently, the Zn^{2+} ion is energetically preferred to transport along the O site to the O site in the channel.[37] However, according to the structural model of CNZT, the arrangement of O atoms along the channels' wall are not even. Specifically, The Zn^{2+} ion diffuses to an adjacent Te atom at a distance of 2.78 Å, and then needs to diffuse an additional 4.85 Å to reach the third Te atom, thus hinders the Zn^{2+} ions transport process. As shown in the RDF curves in Fig. 2c, the O–O coordination distance between the first and second coordination layers of ANZT slightly decreased compared to that of the CNZT sample. The coordination number increases from 6.6 (CNZT) to 8.1 (ANZT). As a result, based on the mean square displacements (MSD, Fig. 2d) curves, the calculated Zn^{2+} ion diffusion coefficient in the channel of CNZT (3.2×10^{-5} A^2 ps^{-1}) is obviously slower than the Zn^{2+} ions in ANZT (5.3×10^{-5} A^2 ps^{-1}). Based on their structure models, Fig. 2e schematically describes the randomly arranged O atoms on the channels, thus reducing the diffusion distance of Zn^{2+} ion in the channels.

In this way, the calculated activation energy for Zn^{2+} ions in the electrolyte to deposit on ANZT@Zn anode is the smallest (25.58 kJ mol^{-1}, Figs. 2f and S6e–g, ESI†). The activation energies on the CNZT@Zn anode and the bare Zn anode are 28.36 and 33.73 kJ mol^{-1}, respectively. Furthermore, the temperature-varied nuclear magnetic resonance (NMR) measurement was also conducted to study the ion transport kinetics in the channels of CNZT and ANZT samples. The full width at half maximum (FWHM) of the signal of NMR spectra is closely associated with the ion diffusion coefficient.[38] Here, the ^{23}Na NMR spectrum is used to substitute the ^{67}Zn NMR spectrum to evaluate the ion diffusion kinetics in channels because of its higher sensitivity to the NMR measurement. As shown in Fig. 2g,h, the FWHM values of ANZT suffer less influence when the test temperatures increase from 0 to 80 °C compared to the CNZT, indicating a larger ion diffusion coefficient.[38] Those above results confirm that the amorphous $Na_2Zn_2(TeO_3)_3$ could effectively enhance the Zn^{2+} ion transport kinetics by enlarging the diameter of channels and reducing the distance for ion diffusion. Note that the signal peak of the ^{23}Na NMR spectrum of the CNZT layer almost disappeared after one Zn plating/stripping cycle (Fig. S7a, ESI†), further confirming the Na^+ ion in channel is replaced by the transported Zn^{2+} ion. Consequently, the Zn metal anode with ANZT interlayer shows the highest Zn^{2+} ion transference number of 0.87 (which of bare Zn and

Journal Name

ARTICLE

CNZT@Zn anodes are 0.58 and 0.75, respectively, Figs. S7b-f, ESI†). Therefore, the ANZT interlayer enables cells the fastest Zn plating/stripping kinetics (the CV curves of half-cells) and the smallest Zn plating/stripping overpotential (the rate performance of symmetry cells, Fig. S8, ESI†) compared to others.

The Electrochemical Performance of Cells with Different Anode

To further determine the superiority of the ANZT interlayer, the ANZT@Zn, ANZT@Cu, CNZT@Zn, CNZT@Cu, bare Zn, and bare Cu electrodes were assembled to Zn||Cu half-cells and Zn||Zn symmetric cells to carry out the electrochemical measurement. For the Zn||Cu half-cells, the bare Cu electrode delivers a low average CE (ACE) of 94.8% at the current density of 1 mA cm^{-2} (Fig. 3a). Surprisingly, the CNZT and ANZT interlayers highly promote the reversibility of the half-cell, as the ACE arrived at 98.6% and 99.2%, respectively. The corresponding charge/discharge curves of the half-cell with bare Cu electrode shows its voltage polarization gradually increase during cycling and then failed after 100 cycles, as displayed in Fig. 3b. In striking contrast, the voltage polarization of the half-cell with ANZT interlayer is almost unchanged even after 500 cycles, emphasizing its outstanding cyclic stability (Fig. 3c). For the cell with the CNZT@Cu electrode, its polarization significantly increases after 200 cycles due to the fast failure of the interlayer (Fig. S9a, ESI†). The smallest corrosion current and the lowest onset potential for HER explain the superior cyclic stability of the Zn||ANZT@Cu half-cell, including the high CE at 5 mA cm^{-2} (Fig. S9b-d, ESI†). In addition, the long-term cycle stability of the Zn||Zn symmetric cells with or without the CNZT and ANZT interlayers is evaluated. As displayed in Fig. 3d, under a current density of 1 mA cm^{-2} with a capacity of 1 mAh cm^{-2}, the ANZT@Zn anode realizes the longest lifespan of 2,790 h, as well as the lowest overpotential among the three Zn anodes. For the CNZT@Zn and bare Zn anodes, they exhibit shorter cyclic lifespans of 962 and 142 h. respectively. In addition, these cells were also tested under high current densities of 9 mA cm^{-2} (with a

capacity of 4.5 mA cm^{-2} and 10 μm Zn foil, Fig. S9e, ESI†) and 20 mA cm^{-2} with a capacity of 5 mAh cm^{-2}. As displayed in Fig. 3e, the bare Zn anode merely sustains for 33 h, while the CNZT@Zn and ANZT@Zn anodes can cycle for 450 and 800 h. In short, as shown in Fig. 3f and Table S2 (ESI†), when compared to the recently reported Zn metal modification strategies, the ANZT interlayer shows the most superior performance.[39]

To determine the potential of the designed ANZT artificial interlayer in the practical application, the Zn||MnO$_2$ and Zn||NH$_4$V$_4$O$_{10}$ cells with ANZT@Zn anode were tested. The CV curves of the ANZT@Zn||MnO$_2$ cell exhibit a smaller polarization than the bare Zn||MnO$_2$ cell, indicating its faster electrochemical reaction kinetics (Fig. S10a, ESI†). Similarly, the charge/discharge curves of the full-cell with the ANZT@Zn anode show a much lower voltage polarization of 305 mV compared to the bare Zn anode (373 mV) and a better rate performance (Fig. S10b,c, ESI†). On the other hand, the long-term cycle stability of those full cells was also tested. The ANZT@Zn||MnO$_2$ cell prevents a discharge capacity of 108.9 mAh g^{-1} after cycling for 1,500 cycles under a current density of 1 A g^{-1} with a capacity retention of 79.2% (Fig. 3g). In contrast, the bare Zn||MnO$_2$ cell occurs fast decay of discharge capacity after 482 cycles and then fails after 610 cycles due to the formation of Zn dendrite (Fig. S10d, ESI†). Furthermore, the Zn||MnO$_2$ cells were also tested under the condition closed to practical application (the N/P ratio reduces to 2.6, Fig. 3h). The ANZT interlayer still endows an excellent cycling performance of the Zn||MnO$_2$ cell. In detail, the cell with ANZT@Zn anode maintains stable cycle for 600 times, which of bare Zn anode is 142 cycles. Meanwhile, the Zn||NH$_4$V$_4$O$_{10}$ cells with different Zn anodes were tested at the current density of 1 A g^{-1} to confirm the universality of the designed ANZT interlayer. As shown in Fig. 3i, the ANZT@Zn||NH$_4$V$_4$O$_{10}$ cell keeps stable cycle for about 1,000 cycles and delivers a discharge capacity retention of 80.1% (336.3 mAh g^{-1}). For the bare Zn||NH$_4$V$_4$O$_{10}$ cell, although it delivers a similar initial discharge capacity as the ANZT@Zn anode, its discharge capacity suddenly reduces after 56 cycles and fails after 513 cycle.
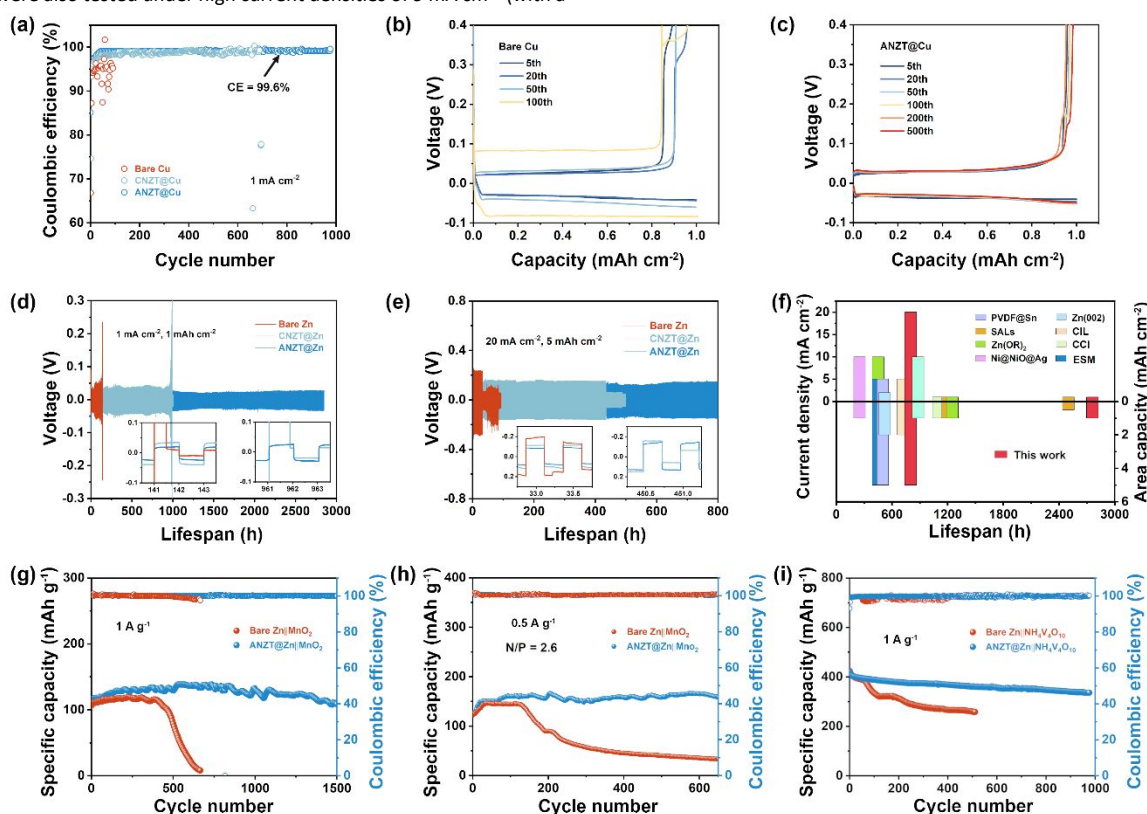
Fig. 3 (a) CE test of Zn||Cu half-cells with bare Cu, CNZT@Cu, and ANZT@Cu electrodes (1 mA cm^{-2}/1 mAh cm^{-2}). Charge-discharge curves of the Zn||Cu half-cells with (b) bare Cu and (c) ANZT@Cu electrodes at the 5th, 20th, 50th, 100th, 200th, and 500th cycles, respectively. Cycle performance of Zn||Zn symmetric cell cycled at a current density of (d) 1 mA cm^{-2} with a capacity of 1 mAh cm^{-2} and (e) 20 mA cm^{-2} with a capacity of 5 mAh cm^{-2}. (f) Compare the cyclic lifespan of ANZT@Zn anode with recently reported anode-modified strategies. Cycling performance of Zn||MnO$_2$ cells at the current densities of (g) 1 A g^{-1} and (h) 0.5 A g^{-1} (10 μm Zn foil, with a low N/P ratio of 2.6). (i) Cycle performance of Zn||NH$_4$V$_4$O$_{10}$ cells with bare Zn and ANZT@Zn anodes at a current density of 1 A g^{-1}.

Study of Zn Deposition Morphology and Interface Stability

The analysis of Zn deposition morphology was carried out to clarify the origin of the excellent stability of the Zn metal anode enabled by the ANZT interlayer. The focused ion beam scanning electron microscopy (FIB-SEM) technology is powerful in studying the micromorphology of deposited Zn metal on Cu electrodes. For the cross-section SEM image of FIB-milled bare Cu electrode (after 2.5 mAh cm^{-2} Zn metal deposited, Fig. 4a), the nucleation and growth of Zn are uneven, thus accelerating the growth of Zn dendrite. On the contrary, as shown in Fig. 4b, the Zn deposition morphology on the ANZT@Cu electrode is uniform and tightly attached to the substrate. Furthermore, the Zn deposition morphologies on different Zn anodes during the Zn plating/stripping cycling were investigated. After 50 cycles at the current density of 5 mAh cm^{-2} with a capacity of 2.5 mAh cm^{-2}, the surface of cycled bare Zn anode is uneven and accompanied by the formation of Zn dendrite (Fig. 4c). Meanwhile, the corresponding enlarged SEM image shows that the orientation of deposited Zn plates is random,

causing the incoherent distribution of electric field and ion flux at the anode interface. In contrast, as displayed in Fig. 4d, the surface of the cycled ANZT@Zn anode is still smooth, and the enlarged SEM images indicate that most of the deposited Zn metal is oriented with the (101) plane, thus delivering a dense Zn deposition morphology. The corresponding side-view SEM images also confirm that the Zn deposition on the bare Zn anode is loose accompanied by many byproducts, whereas that on the ANZT@Zn anode exhibits a remarkably even and compact morphology (Fig. S11a,b, ESI†). In addition, the in-situ optical microscopy measurement was used to further detect the Zn deposition morphology evolution in a large view. Obviously, as displayed in Fig. 4e, some Zn dendrite forms and grows on the bare Zn anode with the continuity of Zn deposition process. For the ANZT@Zn anode, the uniform Zn deposition morphology can be maintained for over 15 minutes, the morphology is dependent on stable Zn^{2+} ion channels and their suppression of the two-dimensional diffusion of Zn^{2+} ions on the anode surface (Fig. S11c, ESI†).
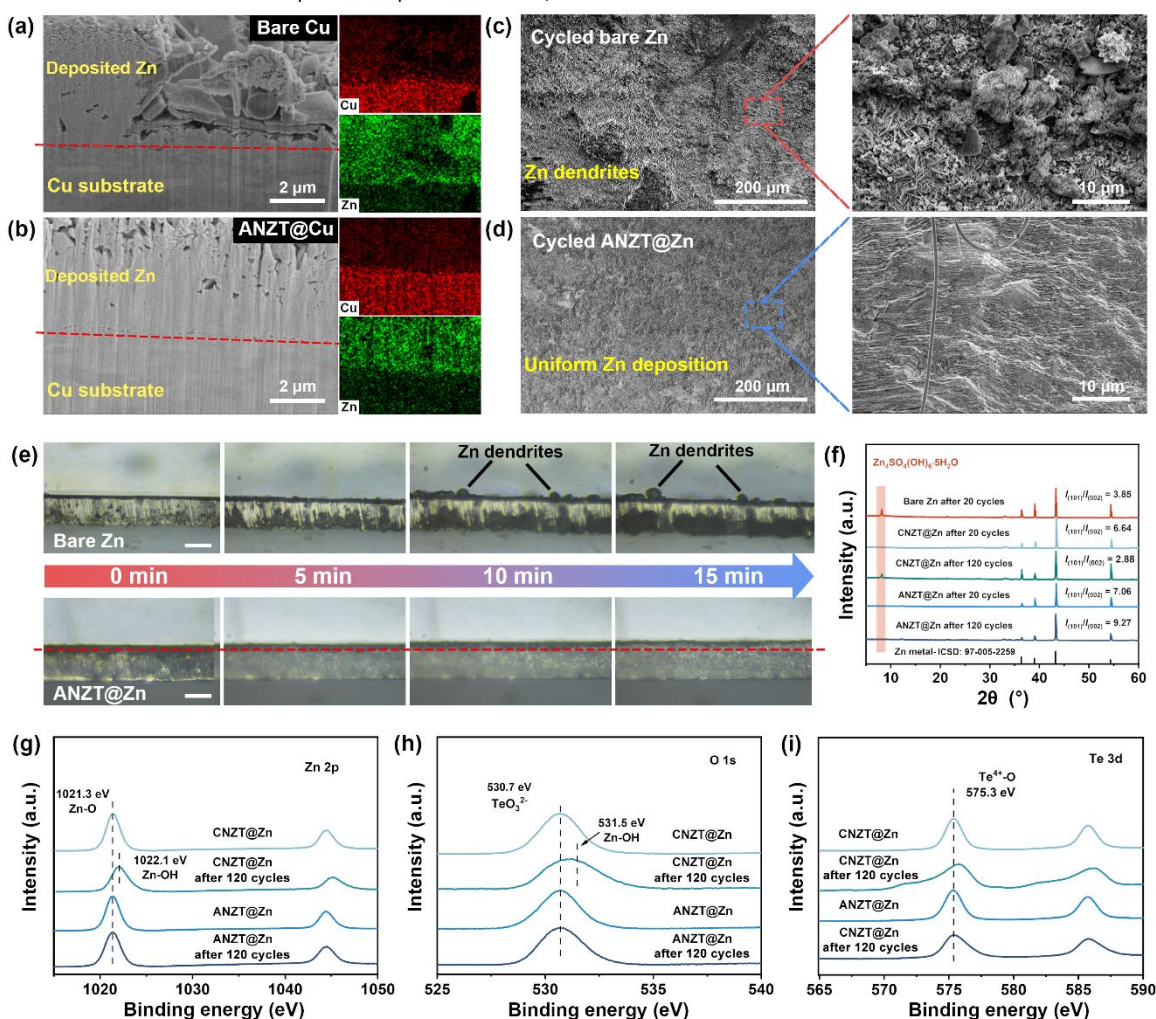
Fig. 4 Side-view SEM images of FIB-milled (a) bare Cu and (b) ANZT@Cu electrodes with 2.5 mAh cm^{-2} Zn metal deposition (at 5 mA cm^{-2}) and the corresponding EDS mapping results. SEM images of (c) bare Zn and (d) ANZT@Zn electrodes after 50 cycles at 5 mAh cm^{-2}/2.5 mAh cm^{-2}, and the enlarged SEM images are inserted at the right. (e) *In-situ* optical microscopy measurement records the Zn deposition morphology on bare Zn and ANZT@Zn anodes (100 μm Zn foil) at a current density of 30 mA cm^{-2}, scale bar: 100 μm. (f) XRD patterns of bare Zn, CNZT@Zn, and ANZT@Zn anodes after different cycle numbers (in symmetric cells at 1 mA cm^{-2}/1 mAh cm^{-2}), with calculated $I_{(002)}/I_{(101)}$ values. High resolution XPS spectra of (g) Zn 2p, (h) O 1s, and (i) Te 3d of CNZT and ANZT interlayers after 120 cycles (in symmetric cells at 1 mA cm^{-2}/1 mAh cm^{-2}).

The XRD patterns of all the bare Zn, CNZT@Zn, and ANZT@Zn anodes after 20 cycles were acquired and displayed in Fig. 4f. Specifically, a diffraction peak at around 8.7° is observed from the bare Zn anode after 20 cycles, corresponding to the $Zn_4(SO_4)_4(OH)_6\cdot5H_2O$.[20] For comparison, this diffraction peak cannot be found on the cycled CNZT@Zn and ANZT@Zn anodes, implying that the side reactions on them are effectively suppressed.

Besides, the values of $I_{(101)}/I_{(002)}$ of bare Zn, CNZT@Zn, and ANZT@Zn are 3.85, 6.64, and 7.08, respectively, indicating that the NZT interlayers could realize the Zn deposition along the (101) crystal plane. Therefore, a compact Zn deposition morphology is achieved on ANZT@Zn surface (as confirmed by SEM image), which effectively reduces the contact area between the Zn anode and electrolyte to inhibit the side reactions.[40] As determined by the

DFT calculation (Fig. S11d, ESI†), the Zn (101) plane shows a higher absorption energy to the TeO_3^{2-} group compared to the Zn (002) and Zn (100) planes, which are 6.54, 1.63, and 2.77 eV, respectively. Therefore, the TeO_3^{2-} group that fixed on the ion channels of the ANZT interlayer can guide the Zn metal deposition along the Zn (101) plane.[41]

When the cycle for 120 times, the diffraction peaks of $Zn_4(SO_4)_4(OH)_6 \cdot 5H_2O$ are still not observed in the XRD pattern of ANZT@Zn anode, and the $I_{(101)}/I_{(002)}$ value increases to 9.27. However, for the CNZT@Zn anode, a weak peak of the byproduct is observed in the XRD pattern, and the $I_{(101)}/I_{(002)}$ value reduces to 2.88. That is, the CNZT interlayer gradually lost its ability to protect the Zn anode during cycling. To clarify it, the XPS measurement of CNZT and ANZT interlayers was conducted to discuss their structure evolution during cycling. As shown in Fig. 4g, the peak located at 1021.3 eV in Zn 2p XPS spectra belongs to the Zn-O bond, which in ANZT interlayer is almost unchanged before and after 120 cycles. For the CNZT interlayer, this peak shifts to a higher binding energy of 1022.2 eV after 120 cycles, which belongs to the Zn-OH bond.[42] As a supplement, the high-resolution O 1s XPS spectra are also acquired, and the peak at 530.5 eV belongs to the anionic $[Zn_2(TeO_3)_3]^{2-}$ skeleton (Fig. 4h). The location of this peak of the ANZT interlayer is almost unchanged before and after 120 cycles, verifying the local structure of the anionic $[Zn_2(TeO_3)_3]^{2-}$ framework is preserved. This peak slightly broadens due to the residue of electrolyte. However, a significantly broad and blue shift happens to the O 1s spectrum of CNZT interlayer after 120 cycles, indicating severe structural destruction and side reaction during cycling. In addition, the Te 3d XPS spectrum of the ANZT interlayer exhibits the same peak location (575.3 eV, belonging to the Te^{4+}–O bond, Fig. 4i) before and after 120 cycles, confirming the Te–O bond of anionic $[Zn_2(TeO_3)_3]^{2-}$ framework is preserved during cycling. In contrast, the Te 3d XPS spectrum of CNZT after 120 cycles shows a broad peak towards high binding energy, indicating the coordination environment of the Te atom is significantly changed. These characterizations all determine

the superior structural stability of the ANZT interlayer, thereby exhibiting the stable charge transfer resistance of the symmetric cell during cycling (Fig. S12, ESI†).

Anion Rejection Behaviour of Designed Interlayer

The negatively charged $[Zn_2(TeO_3)_3]^{2-}$ skeleton of ANZT interlayer can also reject the SO_4^{2-} and I^{3-} anions from the Zn anode surface to avoid the byproducts formation and shuttle effect. In this way, the interlayer can prevent the fast capacity decay when coupled with the iodine cathode. The *in-situ* Raman measurement was carried out on the bare Cu and ANZT@Cu mesh electrodes in a custom mold. As shown in Fig. 5a, during the Zn plating process, a strong peak occurs at about 980 cm^{-1} in the Raman spectra of the bare Cu mesh electrode, which belongs to the vibration of SO_4^{2-}.[16] However, for the ANZT@Cu mesh electrode, only a weak peak can be observed from the Raman spectra during Zn deposition process, implying the side reactions is effectively suppressed (Fig. 5b). As supplementary, the Ar^+-etching XPS measurement was also adapted to study the depth distribution of S element on different Zn anodes that after 50 cycles in the symmetry cells. As displayed in Fig. 5c, the signal peak of the S element could be detected even after 150 nm of Ar^+-etching from the bare Zn anode surface. As a contrast, on the surface of the ANZT@Zn anode, this peak cannot be observed in the S 2p XPS spectrum after Ar^+-etching for merely 50 nm. In addition, the corresponding SEM images and EDS results of the two Zn anodes after cycles were acquired. The content of the S element on the bare Zn anode is 5.6%, which on the ANZT@Zn anode reduced to 0.9% (Fig. S13, ESI†). All the above results verify the excellent ability of the ANZT interlayer in expelling the SO_4^{2-} anions from the Zn anode surface to avoid the formation of byproducts. Consequently, their Ar^+-etching high-resolution XPS spectra (O 1s and Zn 2p) show that the considerable amounts of oxygen-containing byproducts were detected on bare Zn after 150 nm of etching, while cannot be detected on ANZT@Zn anode after 50 nm of etching (Fig. S14, ESI†).
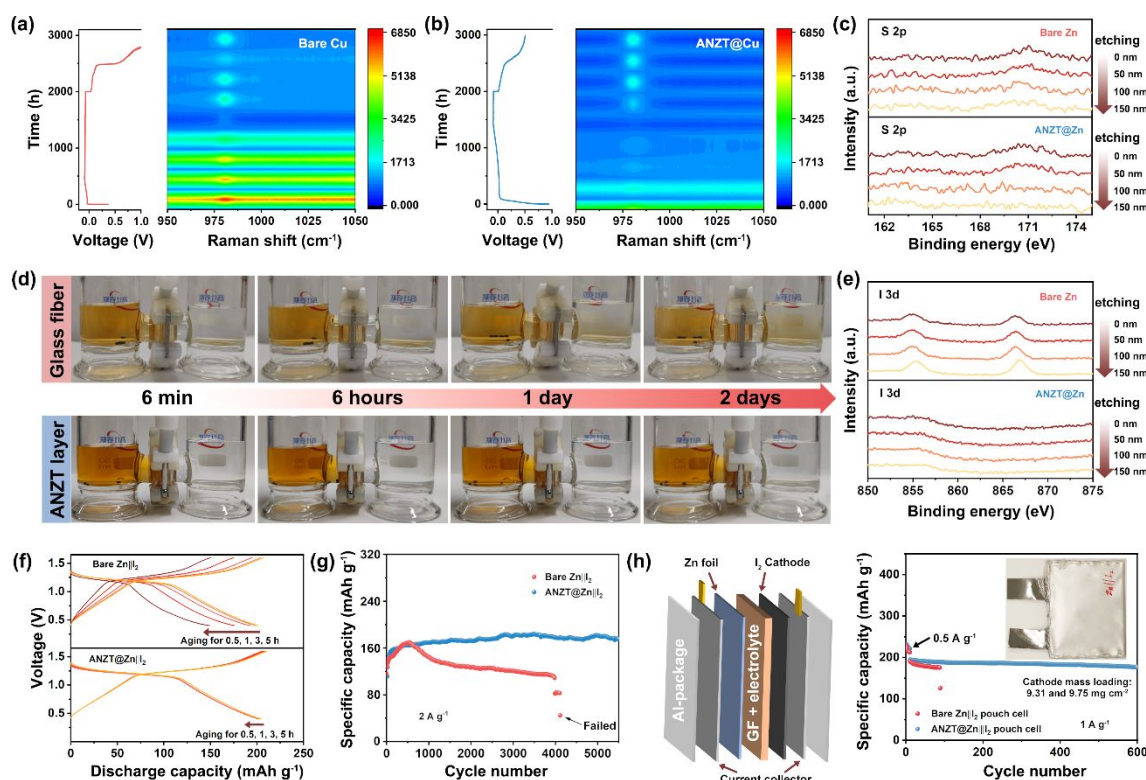
Fig. 5 *In-situ* Raman spectra of (e) bare Cu mesh and (f) ANZT@Cu mesh during the Zn plating/stripping process. (c) The Ar^+-etching high-resolution XPS spectra of S 2p of bare Zn and ANZT@Zn anodes after 50 cycles in the symmetric cells (at 5 mA cm^{-2}/2.5 mA cm^{-2}). (d) Optical images of H-type glass mold with anolyte (left, 0.5 M KIO_3 and 0.1 M I_2), catholyte (0.5 M KIO_3), and the GF separator with/without ANZT coating layer. (e) The Ar^+-etching high-resolution XPS spectra of I 3d of bare Zn and ANZT@Zn anodes after 100 cycles in the Zn||I_2 cells (at 1 A g^{-1}). (f) Electrochemical aging test (from 0.5 to 5 h standing after full charge state) for Zn||I_2 batteries with bare Zn (upper) and ANZT@Zn (lower) anodes. (g) The cycling performance of Zn||I_2 cells with bare Zn and ANZT@Zn anodes at the current density of 2 A g^{-1}. (h) The cycling performance of Zn||I_2 pouch cells with different Zn anodes at the current density of 1 A g^{-1} with the high cathode mass loading of 9.31 (bare Zn) and 9.75 (ANZT@Zn) mg cm^{-2}.

The iodine-diffusion, Raman, and UV/Vis measurements were carried out to confirm the ability of the ANZT interlayer to repel the iodine compound in the electrolyte during cycling. First, we prepared an ANZT layer on the glass matrix, then transferred and attached it to the surface of the glass fiber (GF) separator, named ANZT@GF separator. Those separators were fixed at the middle joint of the H-type glass mold (left: 0.5 M KIO_3 + 0.1 M I_2; right: 0.5 M KIO_3), and left for 6 min, 6 h, 1 day, and 2 days for photographing (Fig. 5d). Clearly, for the H-type glass mold with the GF separator, the iodine-containing yellow solution on the left permeates into the bottom of the right transparent solution after standing for just 6 min. And the solution on the right gradually turns yellow from the bottom up after standing for 2 days. Whereas, for the mold with ANZT@GF separator, the solution on the right remains transparent even after standing for 2 days because of only small amounts of I-contained species permeates through. This result can also be confirmed by the Ar^+-etching XPS of the bare Zn and ANZT@Zn anode after 100 cycles in the Zn||I_2 cell. The high-resolution XPS spectra of I 3d of the cycled bare Zn anode delivers an obvious signal peak even after etching for 200 nm (Fig. 5e). In contrast, benefit from the protection effect of ANZT layer, the signal peak of I 3d can hardly be detected on the ANZT@Zn anode surface. Furthermore, the *ex-situ* Raman and UV/Vis were also used to determine the accumulation of polyiodide compounds on these Zn anodes surfaces during the continuous charge/discharge process. As displayed in Fig. S15 (ESI†), the concentration of I_3^- (the peak locates at 103 cm^{-1} in Raman spectra) on bare Zn anode is significantly increased with the cycle number increased.[41] In contrast, the concentration of I_3^- on the Zn anode under the ANZT interlayer remains at a low concentration. In addition, the concentration of I^- (the peak locates at 220 nm in UV/Vis spectra) on the bare Zn anode also significantly increases during cycling, which on ANZT anode is almost unchanged.[43] In other words, the I_3^- accumulation would cause the incomplete conversion of I_2/I^- and the corrosion of Zn anode, thereby damaging the performance of the Zn||I_2 battery.

The Zn||I_2 full-cell with bare Zn and ANZT@Zn anodes were assembled and tested to evaluate the superiority of the ANZT interlayer. As shown in the CV curve (Fig. S16, ESI†), both the cells with bare Zn and ANZT@Zn anodes exhibits one paired reduction and oxidation peaks. The smaller polarization between redox peaks and higher current of the cell with ANZT@Zn anode compared to bare Zn imply a faster electrochemical reaction kinetics and higher iodine utilization.[44,45] Consequently, it delivers an excellent rate performance under the step-varied current densities from 0.2 to 2 A g^{-1}. Meanwhile, the aging test (Fig. 5f) also confirms the superior performance of the ANZT interlayer in stabilizing the Zn||I_2 cell, as the cell only exhibits a slight decay of the discharge capacity after aging for 5 h. In addition, as presented in Fig. 5g, under the current density of 2 A g^{-1}, the discharge capacity of Zn||I_2 cell with bare Zn anode decays at 580 cycles, and the cell failed after 4,060 cycles. In contrast, the cell with ANZT@Zn anode maintains a stable cycle for more than 5,500 cycles with a capacity retention of 99.3%. Furthermore, these Zn anodes and I_2 cathode were assembled into a pouch cell and tested under the condition that close to practical applications, as shown in Fig. 5h. When the cathode mass loading arrived at 9.75 mg cm^{-2}, after activation for 10 cycles, the ANZT@Zn||I_2 pouch cell still kept a stable cycle for 600 times with a capacity retention of 92.7% at the current density of 1 A g^{-1}. However, bare Zn||I_2 pouch cell shows the fast capacity decay and then failed after 98 cycles, which is ascribed to the magnified polyiodide shuttling and side reactions in the pouch cell compared to the coin cell.[46,47] It worth to mention that the cyclic ability of the assembled pouch cell is superior to recently reported high mass loading pouch cells with different types of cathode materials, including I_2, VO_2, $LiMnO_2O_4$, and NaV_3O_8 (Table S3, ESI†).

Conclusions

In this work, the construction of amorphous zeolite-like $Na_2Zn_2(TeO_3)_3$ interlayer endows the fast electrochemical kinetics of the Zn metal anode. Meanwhile, it realizes the excellent cycling lifespan and reversibility of the Zn anode and the excellent cyclic ability of the zinc-iodine/MnO_2/$NH_4V_4O_{10}$ batteries. Through the elaborate structural characterization, the coordination environment and pore structure of the crystalline $Na_2Zn_2(TeO_3)_3$ sample is confirmed to be preserved in the amorphous one. Besides, based on the MD simulation and ssNMR measurement, both the increased distance of the Te-O bond and the reduced distance between the O atom of the first and second coordination layer help the fast Zn^{2+} ion transport process. Meanwhile, the

constructed interlayer realizes the closely arranged Zn deposition morphology along the Zn (101) plane, thus effectively suppressing the Zn dendrite and water-induced parasitic reactions. It is worth mentioning that the $Zn_2(TeO_3)_3^{2-}$ anion skeleton is verified to repel the SO_4^{2-} and I^- anions from the Zn anode surface, thus suppressing the shuttle effect of the I_2 cathode and inhibiting the corrosion/byproducts on the Zn metal anode. Consequently, the ANZT interlayer achieves a long lifespan of Zn anodes and high Zn deposition/stripping reversibility, including superior electrochemical performances when coupling the modified Zn anode with MnO_2, $NH_4V_4O_{10}$, and I_2 cathodes. In short, our work provides a deep insight into the ion transport mechanism of porous materials and its multiple protective effects for the Zn metal anode to promote the development of high-performance aqueous zinc-ion batteries.

Author Contributions

Conceptualization: Z.J., G.H. Experimental design and investigation: Z.J., Z.D., Y.Z., K.L. Data analyses: Z.J., R.C., H.Y., J.C., Z.C., F.C. Material characterization: Z.J., W.Z., R.P., G.Z. Theoretical simulation: Z.J., S.L. Writing—original draft: Z.J., L.S. Writing—review & editing: Z.J., K.Y., G.H. All authors contributed to discussions of the research.

Conflicts of interest

The authors declare no competing interests.

Data availability

Data availability All data supporting this article have been included as a part of the ESI.†

References

[1] K. C. Yazzie, K. Whyte, S. Begay, J. Glavin, T. Jones, K. Leni-Konig, C. Pratte, D. Madden, D. Reicher, C. B. Field, *Science,* 2024, **384**, 6692.

[2] E. Aramendia, P. E. Brockway, P. G. Taylor, J. B. Norman, M. K. Heun, Z. Marshall, *Nat. Energy,* 2024, **9**, 803–816.

[3] J. Zheng, L. A. Archer, *Sci. Adv.* 2021, **7**, eabe0219.

[4] Y. Liu, X. Lu, F. Lai, T. Liu, P. R. Shearing, I. P. Parkin, G. He, D. J. L. Brett, *Joule*, 2021, **5**, 2845–2903.

[5] Y. Jin, K. Liu, J. Lang, D. Zhuo, Z. Huang, C. Wang, H. Wu, Yi Cui, *Nat. Energy*, 2018, **3**, 732–738.

[6] S. W. D. Gourley, R. Brown, B. D. Adams, D. Higgins, *Joule*, 2023, **7**, 1.

[7] Q. Zhao, M. J. Zachman, W. I. Al Sadat , J. Zheng, L. F. Kourkoutis, L. Archer, *Sci. Adv.*, 2018, **4**, eaau8131.

[8] H. Wu, J. Hao, Y. Jiang, Y. Jiao, J. Liu, X. Xu, K. Davey, C. Wang, S. Qiao, *Nat Commun.*, 2024, **15**, 575.

[9] K. W. Leong, W. Pan, X. Yi, S. Luo, X. Zhao, Y. Zhang, Y. Wang, J. Mao, Y. Chen, J. Xuan, H. Wang, D. Y. C. Leung, *Sci. Adv.*, 2023, **9**, eadh1181.

[10] Z. Cai, H. Wang, T. Wu, H. Ji, Y. Tang, Q. Zhang, Z. Peng, H. Wang, *Mater. Today Energy*, 2024, **43**, 101592

[11] S. Chen, D. Ji, Q. Chen, J. Ma, S. Hou, J. Zhang, *Nat. Commun.*, 2023, **14**, 3526.

[12] L. E. Blanc, D. Kundu, L. F. Nazar, *Joule*, 2020, **4**, 771–799.

[13] J. Yang, T. Xiao, T. Xiao, J. Li, Z. Yu, K. Liu, P. Yang, H. Fan, *Adv. Mater.*, 2024, **36**, 2313610.

[14] J. Hao, S. Zhang, H. Wu, L. Yuan, K. Davey, S. Qiao, *Chem. Soc. Rev.*, 2024, **53**, 4312-4332.

[15] C. Li, S. Jin, L. A. Archer, L. F. Nazar, *Joule*, 2022, **6**, 1727–1742.

[16] W. Zong, J. Li, C. Zhang, Y. Dai, Y. Ouyang, L. Zhang, J. Li, W. Zhang, R. Chen, H. Dong, X. Gao, J. Zhu, I. P. Parkin, P. R. Shearing, F. Lai, K. Amine, T. Liu, G. He, *J. Am. Chem. Soc.*, 2024, **146**, 21377–21388.

[17] L. Zhang, H. Guo, W. Zong, Y. Huang, J. Huang, G. He, T. Liu, J. Hofkens, F. Lai, *Energy Environ. Sci.*, 2023, **16**, 4872-4925.

[18] T. Li, X. Li, H. Yang, Y. Zhou, X. Li, M. Su, A. Dou, P. Zhang, X. Wu, A. Naveed, J. Sumner, Y. Liu, *Mater. Today Energy*, 2024, **40**, 101513.

[19] J. Hu, Z. Zhang, T. Deng, F. Cui, X. Shi, Y. Tian, G. Zhu, *Adv. Mater.*, 2024, **36**, 2401091.

[20] Y. Lyu, J. A. Yuwono, P. Wang, Y. Wang, F. Yang, S. Liu, S. Zhang, B. Wang, K. Davey, J. Mao, Z. Guo, *Angew. Chem.*, 2023, **135**, e202303011.

[21] X. Cai, X. Wang, Z. Bie, Z. Jiao, Y. Li, W. Yan, H. Fan, W. Song, *Adv. Mater.*, 2024, **36**, 2306734.

[22] Z. Cao, H. Zhang, B. Song, D. Xiong, S. Tao, W. Deng, J. Hu, H. Hou, G. Zou, X. Ji, *Adv. Funct. Mater.*, 2023, **33**, 2300339.

[23] F. Wang, J. Tseng, Z. Liu, P. Zhang, G. Wang, G. Chen, W. Wu, M. Yu, Y. Wu, X. Feng, *Adv. Mater.*, 2020, **32**, 200028

[24] Z. Li, X. Wu, X. Yu, S. Zhou, Y. Qiao, H. Zhou, S. Sun, *Nano Lett.*, 2022, **22**, 2538−2546.

[25] C. Xie, Y. Liu, W. Lu, H. Zhang, X. Li, *Energy Environ. Sci.*, 2019, **12**, 1834-1839.

[26] K. Schmidt-Rohr, Q. Chen, *Nature Mater.*, 2008, **7**, 75–83.

[27] W. Xin, J. Xiao, J. Li, L. Zhang, H. Peng, Z. Yan, Z. Zhu, *Energy Storage Materials*, 2023, **56**, 76–86.

[28] Y. Wang, Y. Liu, H. Wang, S. Dou a, W. Gan, L. Ci, Y. Huang, Q. Yuan, *J. Mater. Chem. A*, 2022, **10**, 4366-4375.

[29] C. Zhou, L. Longley, A. Krajnc, G. J. Smales, A. Qiao, I. Erucar, C. M. Doherty, A. W. Thornton, A. J. Hill, C. W. Ashling, O. T. Qazvini, S. J. Lee, P. A. Chater, N. J. Terrill, A. J. Smith, Y. Yue, G. Mali, D. A. Keen, S. G. Telfer, T. D. Bennet, *Nat Commun.*, 2018, **9**, 5042.

[30] R. Miletich, *Monatsh Chem*., 1995, **126**, 417-430.

[31] F. Eder, A. Marsollier, M. Weil, *Mineralogy and Petrology*, 2023, **117**, 145–163.

[32] F. Eder, B. Stöger, M. Weil, *Crystalline Materials*, 2022, **237**, 329–341.

[33] H. Ticha, J. Schwarz, L. Tichy, *Materials Chemistry and Physics*, 2019, **237**, 121834.

[34] G. Lakshminarayana, K. M. Kaky, S.O. Baki, A. Lira, P. Nayar, I.V. Kityk, M.A. Mahdi, *Journal of Alloys and Compounds*, 2017, **690**, 799e816.

[35] Z. Jiang, Z. Du, R. Pan, F. Cui, G. Zhang, S. Lei, G. He, K. Yin, L. Sun, *Adv. Energy Mater.*, 2024, **14**, 2402150.

[36] R. Chen, W. Zhang, C. Guan, Y. Zhou, I. Gilmore, H. Tang, Z. Zhang, H. Dong, Y. Dai, Z. Du, X. Gao, W. Zong, Y. Xu, P. Jiang, J. Liu, F. Zhao, J. Li, X. Wang, G. He, *Angew. Chem.*, 2024, **136**, e202401987.

[37] R. Guo, X. Liu, F. Xia, Y. Jiang, H. Zhang, M. Huang, C. Niu, J. Wu, Y. Zhao, X. Wang, C. Han, L. Mai, *Adv. Mater.*, 2022, **34**, 2202188.

[38] P. Zuo, C. Ye, Z. Jiao, J. Luo, J. Fang, U. S. Schubert, N. B. McKeown, T. Liu, Z. Yang, T. Xu, *Nature*, 2023, **617**, 299–305.

[39] a) Q. H. Cao, Y. Gao, J. Pu, X. Zhao, Y. Wang, J. Chen, C. Guan, *Nat. Commun.*, 2023, **14**, 641. b) Z. Wei, S. Wang, D. Li, S. Yang, S. D. Guo, G. M. Qu, Y. H. Yang, H. Li, *Energy Environ. Sci.*, 2024, **17**, 5440. c) T. Li, S. Hu, C. Wang, D. Wang, M. Xu, C. Chang, X. Xu, C. Han, *Angew. Chem. Int. Ed.*, 2023, **62**, e202314883. d) Y. Gao, Q. Cao, J. Pu, X. Zhao, G. Fu, J. Chen, Y. Wang, C. Guan, *Adv. Mater.*, 2023, **35**, 2207573. e) J. Zhang, W. Huang, L. Li, C. Chang, K. Yang, L. Gao, X. Pu, *Adv. Mater.*, 2023, **35**, 2300073. f) Z. Zheng, D. Ren, Y. Li, F. Kang, X. Li, X. Peng, L. Dong, *Adv. Funct. Mater.*, 2024, **34**, 2312855. g) H. Tian, J. Yang, Y. Deng, W. Tang, R. Liu, C. Xu, P. Han, H. Fan, *Adv. Energy Mater.*, 2023, **13**, 2202603. h) W. Guo, L. Xu, Y. Su, Z. Tian, C. Qiao, Y. Zou, Z. Chen, X. Yang, T. Cheng, J. Sun, *ACS Nano*, 2023, **18**, 10642−10652.

[40] Z. Cheng, K. Wang, J. Fu, F. Mo, P. Lu, J. Gao, D. Ho, B. Li, H. Hu, *Adv. Energy Mater.*, 2024, **14**, 2304003.

[41] R. Al-Gaashani, S. Radiman, A.R. Daud, N. Tabet, Y. Al-Douri, *Ceramics International*, 2013, **39**, 2283–2292.

[42] S. Zhang, J. Hao, H. Wu, Q. Chen, C. Ye, S. Qiao, *Adv. Mater.*, 2024, **36**, 2404011.

[43] M. Kim, J. Yeon, *J. Radioanal Nucl. Chem.*, 2021, **330**, 469–473.

[44] L. Zhang, J. Huang, H. Guo, L. Ge, Z. Tian, M. Zhang, J. Wang, G. He, T. Liu, J. Hofkens, D. J.L. Brett, F. Lai, *Adv. Energy Mater.*, 2023, **13**, 2203790.

[45] Y. Ouyang, W. Zong, X. Gao, S. Leong, J. Chen, Y. Dai, H. Dong, I. Phang, P. Shearing, G. He, Y. Miao, T. Liu, X. Ling, *Angew. Chem. Int. Ed.*, 2025, e202504965. https://doi.org/10.1002/anie.202504965.

[46] L. Zhang, H. Ding, H. Gao, J. Gong, H. Guo, S. Zhang, Y. Yu, G. He, T. Deng, I. P. Parkin, J. Hofkens, X. Fan, F. Lai, T. Liu, *Energy Environ. Sci.*, 2025, **18**, 2462

[47] L. Zhang, K. Luo, J. Gong, Y. Zhou, H. Guo, Y. Yu, G. He, J. Gohy, I. P. Parkin, J. Hofkens, Q. He, T. Liu, K. Müllen, F. Lai, *Angew. Chem. Int. Ed.*, 2025, e202506822, https://doi.org/10.1002/anie.202506822.

Data availability

Data availability All data supporting this article have been included as a part of the ESI.†